The Planetary Science Journal, 5:223 (18pp), 2024 October https://doi.org/10.3847/PSJ/ad71d1

A Detailed Study of Jupiter's Great Red Spot over a 90-day Oscillation Cycle

Amy A. Simon[1], Michael H. Wong[2], Phillip S. Marcus[3], and Patrick G. J. Irwin[4]
[1] Code 690, NASA Goddard Space Flight Center, Greenbelt, MD 20771, USA; amy.simon@nasa.gov
[2] Center for Integrative Planetary Science, University of California Berkeley, Berkeley, CA 94720, USA
[3] Mechanical Engineering Department, University of California Berkeley, Berkeley, CA 94720, USA
[4] Department of Physics, Oxford University, Oxford, OX1 3PU, UK
Received 2024 June 26; revised 2024 August 12; accepted 2024 August 17; published 2024 October 9

Abstract

Jupiter's Great Red Spot (GRS) is known to exhibit oscillations in its westward drift with a 90-day period. The GRS was observed with the Hubble Space Telescope on eight dates over a single oscillation cycle in 2023 December to 2024 March to search for correlations in its physical characteristics over that time. Measured longitudinal positions are consistent with a 90-day oscillation in drift, but no corresponding oscillation is found in latitude. We find that the GRS size and shape also oscillate with a 90-day period, having a larger width and aspect ratio when it is at its slowest absolute drift (minimum date-to-date longitude change). The GRS's UV and methane gas absorption-band brightness variations over this cycle were small, but the core exhibited a small increase in UV brightness in phase with the width oscillation; it is brightest when the GRS is largest. The high-velocity red collar also exhibited color changes, but out of phase with the other oscillations. Maximum interior velocities over the cycle were about 20 m s^{-1} larger than minimum velocities, slightly larger than the mean uncertainty of 13 m s^{-1}, but velocity variability did not follow a simple sinusoidal pattern as did other parameters such as longitude width or drift. Relative vorticity values were compared with aspect ratios and show that the GRS does not currently follow the Kida relation.

Unified Astronomy Thesaurus concepts: Jupiter (873); Atmospheric dynamics (2300); Planetary atmospheres (1244)

Materials only available in the online version of record: animations

1. Introduction

Anticyclonic (high-pressure) rotating vortices exist in many of the planetary atmospheres in our solar system. On the giant planets, large (>5000 km) anticyclones can persist for many decades, while on Earth vortices and eddies last a few years at most (Schultz Tokos K. & T. Rossby 1991). The best-known and longest-lived anticyclone is Jupiter's Great Red Spot (GRS; e.g., B. M. Peek 1958; J. H. Rogers 1995; A. A. Simon-Miller et al. 2002; X. S. Asay-Davis et al. 2009; S. Shetty & P. S. Marcus 2010; A. A. Simon et al. 2018; A. Sánchez-Lavega et al. 2024). Similar large vortices on Neptune, such as the Voyager Great Dark Spot (GDS) and others observed since, last only a few years as they drift in latitude or simply fade away (H. B. Hammel et al. 1995; A. Hsu et al. 2019; M. H. Wong et al. 2022). In contrast, Jupiter's alternating zonal wind field anchors the GRS in latitude, perhaps contributing to its extreme longevity.

Earth's vortices are also disrupted by changes in latitude (Coriolis forces) or by forces that lead to instability (e.g., landfall, upper-level wind shear); only rare mid-Atlantic eddies last longer than a year (G. G. Sutyrin 2020). However, terrestrial eddies have been extensively studied, showing they dissipate as the mid-level core of the storm erodes over time, but intensifying internal winds can increase their longevity (K. Schultz Tokos & T. Rossby 1991; G. G. Sutyrin 2020). While such measurements are not possible for Jovian vortices, other peculiar behaviors have been observed over various time periods. For example, the GRS drifts westward relative to Jupiter's wind field but with a ~90-day oscillation in the absolute drift rate (e.g., H. G. Solberg 1969; J. M. Trigo-Rodriguez et al. 2000; R. Morales-Juberias et al. 2022). On Neptune, Voyager 2 observed a smaller dark spot that oscillated in both latitude and longitude, while the larger GDS also oscillated in shape (H. B. Hammel et al. 1995; L. A. Sromovsky et al. 2002; M. H. Wong et al. 2018).

Oscillations and waves are a typical response to perturbations in a flow, as the system returns to balance (e.g., J. Holton 1992). Numerical and analytical studies have shown that a vortex's aspect ratio and axis angle relative to latitude lines are balanced by its vorticity (velocity change over distance) relative to that of the background wind field. Known as the "Kida relation" (S. Kida 1981; L. M. Polvani et al. 1990), this behavior was clearly observed in Neptune's GDS (R. Lebeau & T. E. Dowling 1998). While the Kida relation neglects vertical structure or other balancing mechanisms (A. Ingersoll et al. 2004), it does give interesting first-order insight into oscillations and is worth considering. During the Voyager era, the GRS's aspect ratio and wind measurements were broadly consistent with this relationship, though those measures did not exhibit oscillations that would have been conclusive (A. Ingersoll et al. 2004; A. Sánchez-Lavega et al. 2021).

Jupiter's atmospheric flow can be considered to be quasi-geostrophic, where Coriolis forces nearly balance pressure gradients (e.g., T. E. Dowling 1995; P. Read et al. 2006a). Quasi-geostrophic potential vorticity is the sum of the planetary vorticity, relative vorticity, and stretching vorticity (e.g., J. Holton 1992). In a rotating fluid, a change in relative vorticity can be balanced by stretching vorticity, evidenced by

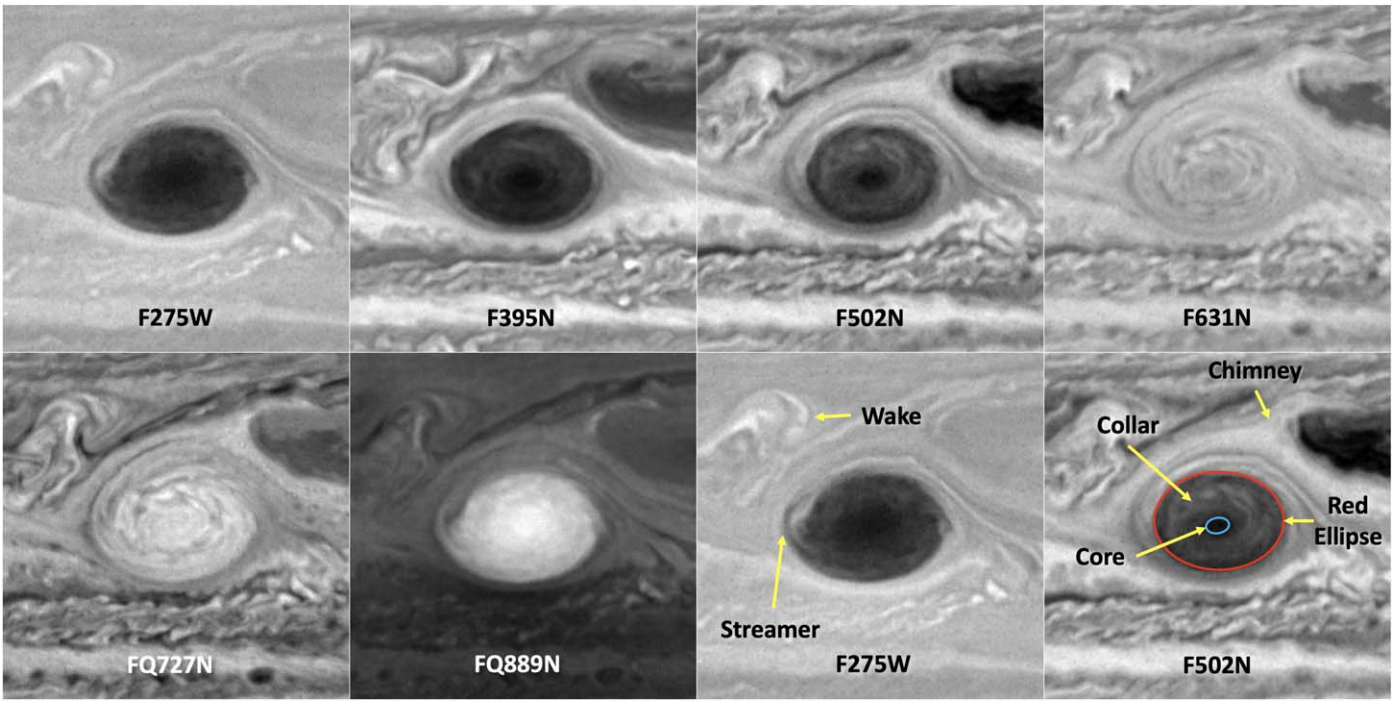

Figure 1. The GRS's appearance at wavelengths from 275 to 889 nm on 2023 December 10. The GRS is dark in the UV (F275W), violet (F395N), and green (F502N) filters but shows little contrast at red wavelengths (F631N). The methane absorption bands (FQ727N and FQ889N) are sensitive to clouds at different tropospheric altitudes, but not as high as in the UV, which is sensitive to stratospheric haze. Common features are labeled for reference.

a change in vortex altitude extent, as the quasi-geostrophic potential vorticity is conserved in the absence of other vorticity sources (J. Holton 1992; P. Read et al. 2006a). A growing vertical extent (at the vortex top and/or bottom) would also mean increased exposure to vertical wind shear (P. J. Gierasch et al. 1986; L. Li et al. 2006), which can act to eventually shear a vortex apart, as has been observed in terrestrial cyclones. Prior Hubble Outer Planet Atmospheres Legacy (OPAL) observations in 2015–2018 found that an increased internal velocity appeared to be accompanied by an increase in FQ889N brightness (A. A. Simon et al. 2018). However, those coarse observations (once per year) were insufficient to discern if any observed cloud-top altitude changes are only transient as the spot adjusts, for example during an oscillation cycle; it is not possible to directly measure commensurate changes at the bottom of the GRS.

At the cloud-top level, the more than 150 yr long observational record also shows that the GRS has decreased in horizontal size substantially, with a size change visibly evident even in the past 20 yr (A. A. Simon-Miller et al. 2002; D. Choi et al. 2007; X. S. Asay-Davis et al. 2009; S. Shetty & P. S. Marcus 2010; A. A. Simon et al. 2018; A. Sánchez-Lavega et al. 2024). Recent Cassini, Hubble, and ground-based data confirm that the 90-day longitude oscillation still holds despite the GRS's smaller size (J. M. Trigo-Rodriguez et al. 2000; R. Morales-Juberias et al. 2022). It should be noted that the GRS is still larger than the corresponding latitude band defined by the wind field, causing the wind jets to deflect around it (A. A. Simon et al. 2018). However, as the GRS has shrunk in both longitude and latitude, its interactions with the surrounding wind field have become more complex. Evidence of such interactions are observed in changes around the periphery of the GRS, especially at higher altitudes, visible in the UV and methane gas absorption bands; see Figure 1 (A. Sánchez-Lavega et al. 2021; M. H. Wong et al. 2021).

The GRS is bounded by the westward wind jet at $-19.5°$ and the eastward wind jet at $-26.5°$ planetographic latitude. The local wind jets deflect around the spot resulting in distinct cloud patterns, including a turbulent region to the northwest of the GRS called the "wake." The local flow partially recirculates to the adjoining wind jets as it encounters the GRS, but some of it passes by to the north or south, and the remainder encounters the GRS's flow pattern along its external white collar of material (e.g., J. L. Mitchell et al. 1981; J. H. Rogers 1995; P. V. Sada et al. 1996). How much material enters the flow, or deflects, varies, but is marked by the presence of a "chimney" in the clouds, which is sometimes described in amateur images as "open" or "closed" (Figure 1). For clouds that enter the GRS flow, entrainment of material into the GRS usually occurs on the southeast side. However, in recent years increased levels of cloud material from the jets have also been seen entering the GRS flow field on the north and west sides (Figure 1).

Other prominent features of the GRS include a dark core surrounded by a high-velocity collar. The GRS collar is also not uniformly red and can brighten when fresh clouds are ingested (e.g., P. V. Sada et al. 1996). Darker collar features, some of which are chevron-shaped, have been historically used to manually measure the high-velocity collar (J. L. Mitchell et al. 1981; A. A. Simon-Miller et al. 2002). However, these dark features were noted to have changed character, starting in 2014, increasing in contrast over a more extended region (A. A. Simon et al. 2018; A. Sanchez-Lavega et al. 2018). Starting in 2018, dark features have also appeared on the very edge of the red ellipse (A. Sanchez-Lavega et al. 2018).

In this study, we analyzed the properties of the GRS over a 90-day oscillation period using a series of Hubble image sets collected from early 2023 December through early 2024

Table 1
Hubble Data[a]

Date	Time Elapsed (days)	Orbits	Observation Time Intervals[b]	Notes
2023 Dec 10	0.0	3	∼30 minutes, 90 minutes, and 10 hr	
2023 Dec 28	18.2	2	∼30 minutes and 10 hr	
2024 Jan 6	26.9	4	∼30 minutes, 90 minutes (2), and 10 hr	OPAL, no FQ727
2024 Jan 12	32.7	3	∼30 minutes, 90 minutes, and 10 hr	
2024 Jan 31	52.2	3	∼30 minutes, 90 minutes,and 10 hr	
2024 Feb 12	63.7	3	∼30 minutes, 90 minutes, and 10 hr	
2024 Feb 24	76.6	2	∼30 minutes and 10 hr	No FQ727
2024 Mar 8	88.5	2	∼30 minutes and 10 hr	No FQ727

Notes.
[a] Data can be found online at MAST doi:10.17909/e04n-w807.
[b] Observations within an orbit last about 30 minutes and orbits were separated by either 90 minutes or ∼10 hr.

March. Section 2 describes the data used and processing performed for each date. Section 3 reports on the position of the GRS over this period, as well as its drift rate, setting the phase of the oscillation. In Section 4, the GRS's size and shape are measured based on visible cloud features, as well as the dynamical (wind) field. Section 5 examines the brightness variations of the GRS core and highest-velocity collar, defined in Figure 1, to look for any evidence of cloud altitude/color changes with oscillation phase. In Section 6, we analyze the cloud-deck-level flow patterns in and around the GRS to find the mean characteristic velocity and the mean relative vorticity throughout the 90-day oscillation. Section 7 examines the relative cloud structure variations in and around the GRS over the oscillation cycle. Lastly, Section 8 discusses the amplitude of the oscillations with respect to the wind field and compare with expectations from the Kida relation.

2. Observations and Data Processing

The Hubble data in this program were captured over a single 90-day oscillation period, using the Wide Field Camera 3 (WFC3) UVIS channel; see Table 1. The data were intended to be acquired as close to opposition as possible, for maximum spatial resolution, using six filters (F275W, F395N, F502N, F631N, FQ727N, and FQ889N). For time-separated velocimetry retrievals of the GRS wind field, as well as some viewing-angle coverage for cloud structure analysis, the visits were designed to be executed in three Hubble orbit sets: two contiguous Hubble orbits and another orbit approximately 10 hr before or after. However, due to telescope operational constraints, the program was executed later than planned, and in some cases only two orbits could be obtained while maintaining guide-star coverage, and some filters were also dropped when needed (Table 1). This resulted in better time coverage over the 90-day period, but at the expense of some cloud structure coverage or short-time-separation wind pairs. Fortuitously, Hubble Jupiter data were also obtained by the OPAL program (A. A. Simon et al. 2015) during our campaign and were included in the analyses where possible.

All data were processed in the standard WFC3 calibration pipeline. The images were further post-processed to remove cosmic rays, and to better remove the residual fringing in the narrowband long-wavelength filters, typically a 2%–3% improvement (M. H. Wong 2011). All images were navigated with planetary ephemeris information using iterative ellipsoid limb fitting to find planet center and absolute latitude and longitude coordinates. For the size, shape, and color analyses, the images were then mapped at 0.1° pixel^{-1} spatial resolution, as in Figure 1. To convert to intensity/flux (I/F), the filter- and time-dependent calibration coefficients (PHOTFLAM) from the image headers were used, along with the integrated solar flux over the bandpass (see A. A. Simon et al. 2015, for further details). This results in an absolute calibration uncertainty of 2% in most filters and 5% in the FQ889N. Figure 1 shows the typical GRS appearance in each of the acquired filters, as well as labeling some features that will be discussed through this manuscript.

We also created maps using red-filter data (F631N, with additional F658N frames for the OPAL data set) spanning planetographic latitudes 40°S to 5°S, and 50° of longitude roughly centered on the GRS at each epoch as inputs for the Advection-Corrected Correlation Image Velocimetry (ACCIV) tool for velocity extraction (X. S. Asay-Davis et al. 2009; X. S. Asay-Davis 2015). ACCIV was designed to accurately measure vortex velocity fields by creating an initial velocity field using short-time-separation (within a single Jupiter rotation) data. Final velocity fields are then created using long-time-separation (consecutive Jupiter rotations) data, by measuring correlations between image maps advected to a common time point using the initial, crude velocity field. Additional iterations of advection-correlation were then conducted to reduce errors. The approach has been effectively used on OPAL data (M. H. Wong et al. 2021), where a series of consecutive Hubble Space Telescope (HST) orbits provide ample data at short time separations, typically ∼80 minutes. For this project, we used 2–3 HST orbits over two Jupiter rotations to efficiently span a 90-day GRS oscillation while minimizing total orbit allocation. While this observational approach resulted in excellent short-time-separation intervals of 95 minutes for four epochs, some epochs produced short-time-separation image pairs of only 28 minutes, or in some cases only 18 minutes. Because retrieved velocity errors scale with the displacement divided by the time interval, these short intervals produced significant errors that were then propagated into the final velocity field via the advection process. Parameters for the ACCIV passes, input and output files, and analysis summaries for each epoch are archived in a larger GRS MAST repository (M. H. Wong 2021).

With consecutive orbits spanning two Jupiter rotations in the OPAL data set, the January 5 velocity field was the only ideal case, with more than ∼90 minutes maximum time separations in both the first and the second Jupiter rotation. For the December data sets, only 28 minutes separations were available (single image pairs in each Jupiter rotation), and for December

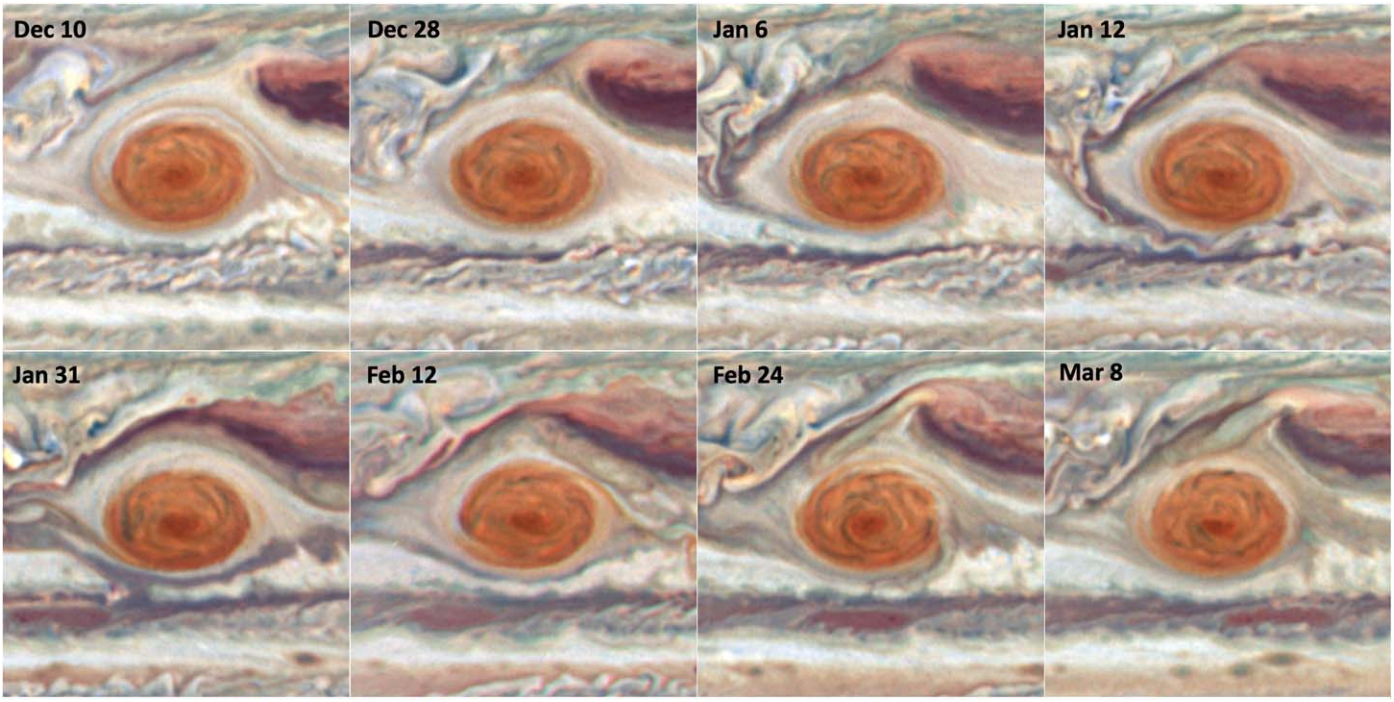

Figure 2. Enhanced color composite maps for each date analyzed. The composites use the F631N (R), F502N (G), and F395N (B) filters, and have been further enhanced with an unsharp mask to bring out details. Each map spans ±15° of latitude and longitude, centered on −23° planetographic latitude and the GRS longitude. Note the open "chimney" above the GRS on December 10, February 24, and March 8. An animation of this sequence is available online (Figure A4 in the Appendix).

28, only the second Jupiter rotation could be used to create an initial velocity field. For January 12, January 31, and February 12, the first Jupiter rotation provided up to ∼95 minutes of time separation, but only January 12 could also provide a short-time-separation image pair of 28 minutes in the second rotation. For February 24 and March 7, ∼35 minutes time separations were available, but rotation 1 on February 24 had only an 18 minutes time separation available, and ultimately no reliable velocity field could be obtained on this date.

To characterize the final velocity fields, we followed the automated process in M. H. Wong et al. (2021) to obtain the size and position of the best-fit ellipse describing the ring of high-speed velocities in the GRS and differentiated the gridded velocity field to obtain relative vorticities. The relative vorticity calculation focuses on the vorticity specific to the vortex, so we subtracted the OPAL 2020 zonal wind profile from every velocity field. To characterize the mean speed in the high-speed ring, we used two methods: the "ellipse method," which calculates an average over vectors near the best-fit ellipse, and the "spokes method," which finds the maximum velocity on a series of spokes radiating from the GRS center, then calculates the average of these maxima (M. H. Wong et al. 2021). Measurements made from the velocity field vectors are denoted as "dynamical" longitude, size, etc., in the subsequent analyses, to distinguish these parameters from the "photometric" longitude, size, etc., based on the direct imaging data (Section 3).

3. GRS Position Measurements

The size and location of the GRS were historically measured using the boundaries of its red edges (e.g., B. M. Peek 1958; J. H. Rogers 1995; A. A. Simon et al. 2018), as seen in Figure 2. Although the GRS is darker at violet wavelengths, the edges can be somewhat obscured by the frequent streamers of red material, especially in the past few years (A. Sánchez-Lavega et al. 2021). The GRS edges in the F502N filter are least affected by the streamers (Figure 1), and were used for manual measurements to define the east, west, north, and south edges along the central spot axes, though determination of the edge locations can be somewhat subjective. These measures are typically used to calculate the central planetographic latitude and longitude, as well as size. However, even the F502N filter was affected by streamers on some dates (Figure 3), increasing the uncertainty on the exact edges that define the spot. Finding the precise GRS edges is not a problem for size and longitude trending over very long time periods or when many measurements, even from different methods or observers, can be used to overcome the uncertainty in edge location, for example trending from frequent amateur image archives (R. Morales-Juberias et al. 2022). However, when searching for variations over very short intervals with sparse data, this lack of precision can dominate the analysis.

Because streamers and irregular edges affect the precision of location measurements, we adopted an alternate definition of the central GRS longitude as the center of the dark core; see Table 2. To determine the GRS edge and colored-cloud center latitudes, we visually identified the continuous ellipse centered on the core longitude (see Figure A1) that best encompassed the outer colored region; note that the core latitude is not always in the center (i.e., the center of the core and red ellipse differ). The ellipse method gave very similar results to manual measurements for edge locations, except on February 12, when it was difficult to visually define the southern edge because of the streamer material entering the GRS; on the southern edge, the ellipse method gave −26.3° latitude, between the manually measured extremes of −26.1° and −26.9° latitude, depending on if the streamer is included.

Another method of finding the GRS center is the identification of the high-speed velocity collar interior to the spot itself using automated velocimetry as discussed above. This

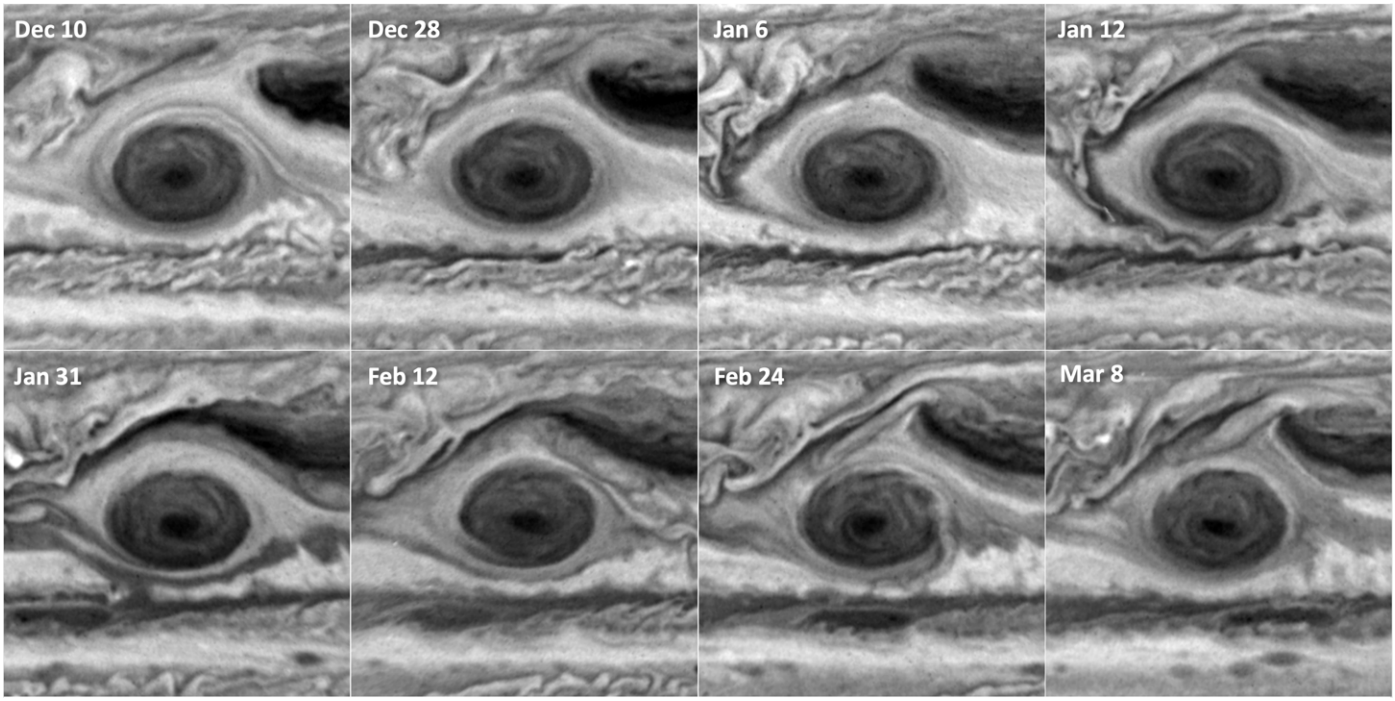

Figure 3. GRS maps in the F502N filter for each date. Note the separated southern edge on February 12, as well as ragged edges on many other dates. Each map spans ±15° of latitude and longitude, centered on −23° latitude and the GRS longitude.

Table 2
GRS Position Parameters (in Planetographic Latitude and System III W. Longitude)

Date	Core			Red Ellipse			Dynamical		
	Long. (deg)	Lat.[a] (deg)	Drift Rate (deg day^{-1})	N. Lat.	S. Lat. (deg)	Center Lat. (deg)	Long. (deg)	Lat.[b] (deg)	Drift Rate (deg day^{-1}) (deg)
2023 Dec 10	95.6 ± 0.1	−23.1 ± 0.1	⋯	−18.5 ± 0.1	−26.9 ± 0.1	−22.7 ± 0.1	95.7 ± 0.1	−21.9 ± 0.3	⋯
2023 Dec 28	101.8 ± 0.1	−23.1 ± 0.1	0.347 ± 0.011	−18.3 ± 0.1	−27.0 ± 0.1	−22.7 ± 0.1	102.0 ± 0.1	−24.3 ± 0.5	0.347 ± 0.011
2024 Jan 6	104.5 ± 0.1	−23.2 ± 0.1	0.303 ± 0.023	−18.6 ± 0.1	−26.9 ± 0.1	−22.7 ± 0.1	104.2 ± 0.1	−22.6 ± 0.1	0.252 ± 0.023
2024 Jan 12	106.0 ± 0.1	−23.3 ± 0.1	0.259 ± 0.035	−18.2 ± 0.1	−26.9 ± 0.1	−22.6 ± 0.1	105.7 ± 0.1	−22.2 ± 0.1	0.259 ± 0.035
2024 Jan 31	111.2 ± 0.1	−23.4 ± 0.1	0.270 ± 0.010	−18.6 ± 0.1	−26.9 ± 0.1	−22.7 ± 0.1	111.0 ± 0.1	−23.2 ± 0.2	0.273 ± 0.010
2024 Feb 12	114.8 ± 0.1	−22.9 ± 0.1	0.308 ± 0.017	−18.0 ± 0.1	−26.3 ± 0.3	−22.2 ± 0.3	114.7 ± 0.1	−22.2 ± 0.5	0.321 ± 0.017
2024 Feb 24	119.0 ± 0.1	−23.2 ± 0.1	0.323 ± 0.016	−18.3 ± 0.1	−26.9 ± 0.1	−22.6 ± 0.1	⋯	⋯	⋯
2024 Mar 8	123.2 ± 0.1	−23.5 ± 0.1	0.346 ± 0.017	−18.2 ± 0.1	−26.7 ± 0.1	−22.4 ± 0.1	123.2 ± 0.1	−22.8 ± 0.1	0.342 ± 0.008

Notes.
[a] All latitudes are planetographic.
[b] Dynamical latitude is computed using the extended velocity field, which can skew the value. The corresponding mean wind velocity magnitude ellipses are centered at −22.5° on all dates.

computational method is not dependent on visual identification and the cloud brightness contrast of an edge, and is therefore a less subjective interpretation of which features mark the extent of the storm (e.g., A. A. Simon et al. 2018; M. H. Wong et al. 2021). Using this method on each of our dates, we also identify the GRS's dynamical position (Table 2; see also Section 6). Although the central latitude was found from the extended velocity fields, the mean velocity ellipse central latitude was −22.5° latitude.

The 90-day oscillation is best shown in the GRS's longitude and drift rate (the longitude rate of change relative to the planetary rotation); see Figure 4. The long-term drift rates shown in Figure 4 (upper right) were calculated by subtracting the GRS's location on 2023 January 13 (350.5°W) and 2023 September 9 (64.4°W) from the central longitudes in Table 2 and dividing by the time elapsed (both dates are from Hubble program GO17275). We assumed a conservative ±0.2° uncertainty in relative positions to compute all error bars. A sinusoidal oscillation is visible in these drifts, but the exact phase is dependent on the time baseline for the longitude displacements. To set the oscillation phase for our subsequent analyses, we also calculated the absolute drift rates between

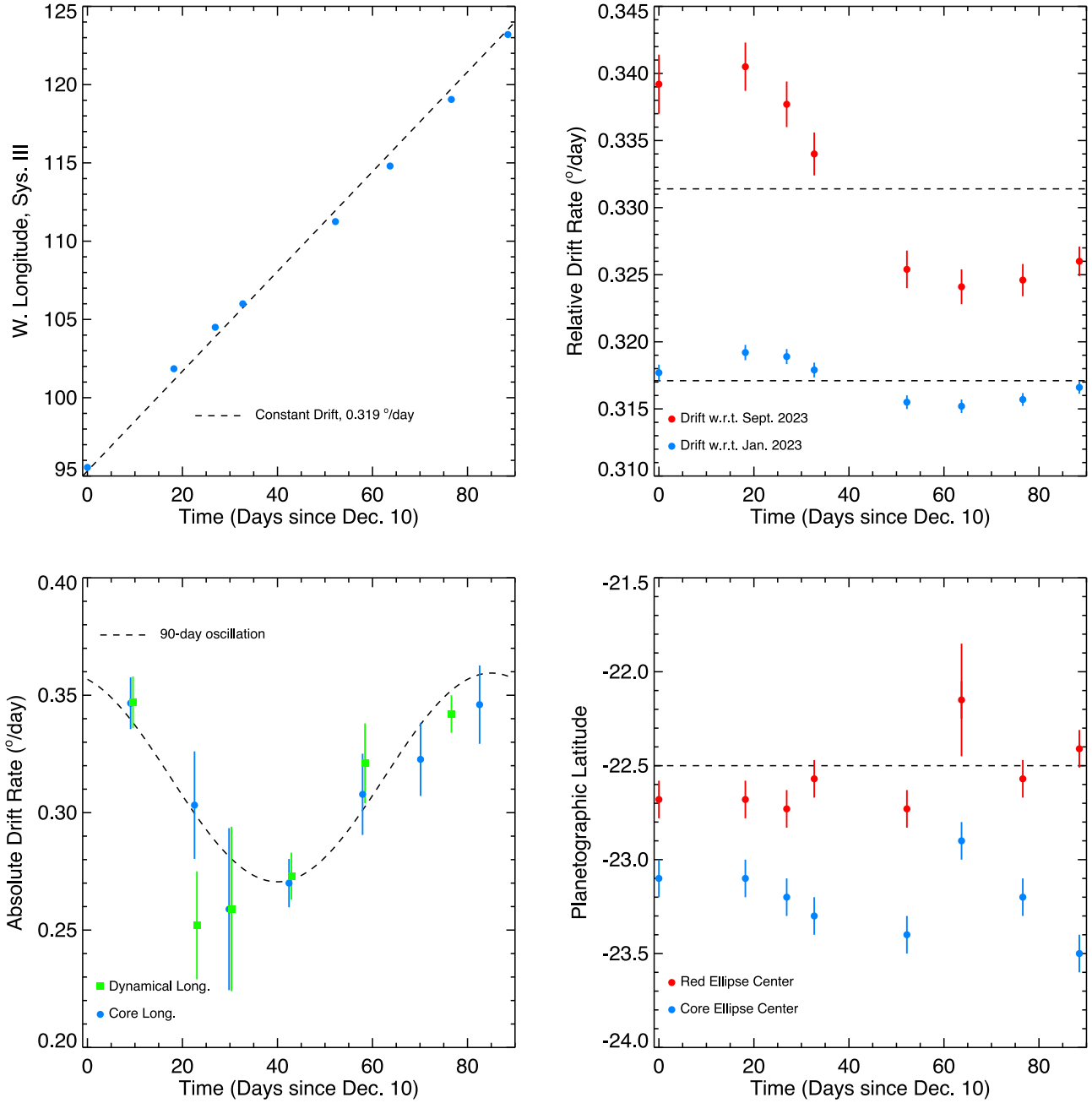

Figure 4. The GRS position over time. Top left: the GRS longitude from December 10 to March 8 shows a small oscillation when compared with the position expected from a constant drift rate of 0.319° day^{-1} (dashed line); uncertainties are smaller than the symbol size. Top right: the variations in drift rate are more apparent when plotted against a fixed time and location, 2023 January 13 (blue points) and 2023 September 9 (red points); the longer time base dilutes the variations. Bottom left: the absolute drift rates between each date show large variations in drift rate and set the phase of the 90 days oscillation. The dynamical data (offset by 0.5 day for clarity) agree with the measured core data, except for December 28. Bottom right: the GRS central and core latitudes also vary, but do not show any 90 days oscillation; the dashed line indicates the dynamical mean latitude.

each observation in Table 1 using the core and dynamical longitude positions. Although the oscillation period can vary somewhat from 90 days (R. Morales-Juberias et al. 2022), with only one cycle of data we cannot reliably fit a period. However, we find a 90-day oscillation fits the drift rates with a Pearson correlation coefficient r of 0.94. Similar plots of GRS central and core latitudes do not show evidence of an oscillation.

4. GRS Size and Shape

As the visually identified red cloud size is still somewhat subjective, those ellipses were also compared with brightness contours. These showed no appreciable difference in size or shape, except on February 12 and 24, when the contours were too ragged to follow. The ellipse method is less dependent on variations around the exterior and more consistently finds the edges than manual measurement or contours, so we adopt this technique for the overall GRS size and shape values in Table 3. However, for the core itself, the size and shape are not as easily visually separated and identified. For detailed core measurements, we used the ellipse that best matched the constant brightness contours; see Figure A2.

As seen in Table 3, all measures of the GRS size vary over time. From the red cloud ellipse data, the GRS width

Table 3
GRS Size and Shape Parameters

Date	Core			Red Ellipse			Dynamical Ellipse		
	Major Axis (km)	Minor Axis (km)	Aspect Ratio	Major Axis (km)	Minor Axis (km)	Aspect Ratio	Major Axis (km)	Minor Axis (km)	Aspect Ratio
2023 Dec 10	3118 ± 118	2084 ± 117	1.50 ± 0.02	13332 ± 118	9801 ± 117	1.36 ± 0.02	12803 ± 1240	10772 ± 611	1.19 ± 0.13
2023 Dec 28	3876 ± 118	2084 ± 117	1.86 ± 0.02	13654 ± 118	10115 ± 117	1.35 ± 0.02	10726 ± 1280	9774 ± 1159	1.10 ± 0.18
2024 Jan 6	3961 ± 118	2167 ± 117	1.83 ± 0.02	14040 ± 118	9738 ± 117	1.44 ± 0.02	11132 ± 353	8845 ± 143	1.26 ± 0.04
2024 Jan 12	4045 ± 118	2250 ± 117	1.80 ± 0.02	13911 ± 118	10178 ± 117	1.37 ± 0.02	10970 ± 342	9136 ± 24	1.20 ± 0.05
2024 Jan 31	4298 ± 118	2584 ± 117	1.66 ± 0.02	14233 ± 118	9738 ± 117	1.46 ± 0.02	11848 ± 472	8871 ± 272	1.34 ± 0.07
2024 Feb 12	4466 ± 118	2250 ± 117	1.98 ± 0.02	13589 ± 118	9613 ± 117	1.41 ± 0.02	11500 ± 681	9623 ± 1172	1.20 ± 0.16
2024 Feb 24	3708 ± 118	2334 ± 117	1.59 ± 0.02	13267 ± 118	10053 ± 117	1.32 ± 0.02	…	…	…
2024 Mar 8	4045 ± 118	1834 ± 117	2.21 ± 0.02	12881 ± 118	9927 ± 117	1.30 ± 0.02	11309 ± 568	9372 ± 146	1.21 ± 0.06

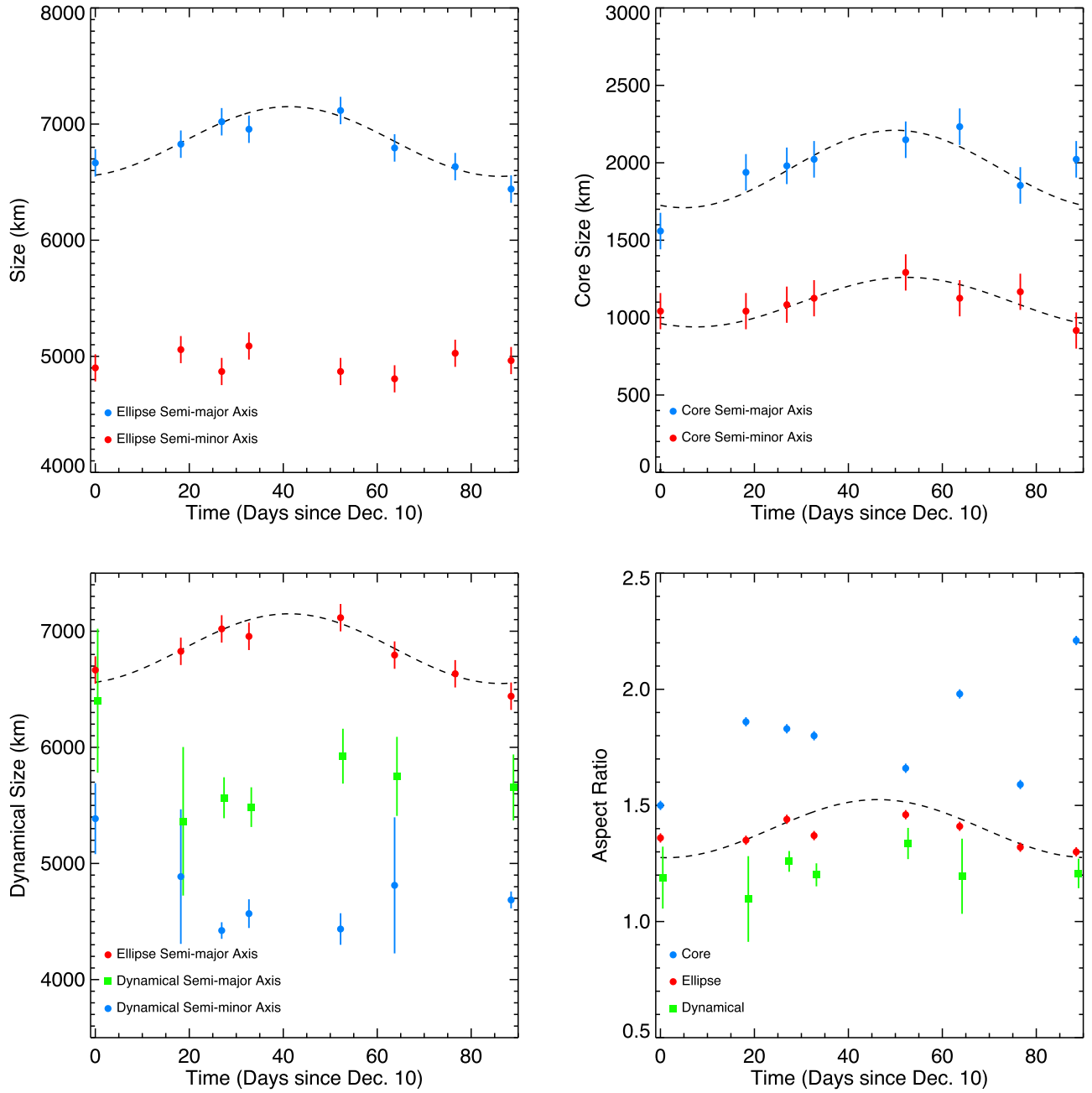

Figure 5. GRS size variation over time. Top left: GRS size from visually identified elliptical red cloud boundaries. Top right: GRS core size from smoothed (elliptical) brightness contours. Bottom left: dynamical size based on the velocity field, with the red cloud size overlaid for comparison; dynamical semimajor axis data are offset by 0.5 day for clarity. Bottom right: aspect ratios (major/minor axes) from the measures in the other three panels; dynamical aspect ratio data are offset by 0.5 day for clarity.

shows evidence of the 90-day oscillation, $r = 0.93$, nearly anticorrelated with the drift rate oscillation (phase lag of 175°); see Figure 5. The GRS minor axis shows little correlation, $r < 0.5$, with a 90-day oscillation. The core size also shows evidence of an oscillation in both dimensions; the major axis shows moderate correlation, $r = 0.73$, while the minor axis is more strongly correlated, $r = 0.84$. For the dynamical sizes, only the minor axis showed an oscillation correlation with $r > 0.7$; for several epochs, the uncertainties are larger than the expected maximum amplitude of the variability (Figure 5). The major-to-minor aspect ratio follows the trends of their respective measures, though the dynamical aspect ratio now appears more similar to that from the red ellipse sizes. The red ellipse aspect ratio shows a correlation with a 90-day oscillation with $r = 0.81$ with a phase lag of 155° from the drift oscillation, unsurprisingly, as it is largely driven by the width oscillation.

5. GRS Brightness Variations

As seen in Figure 1, the GRS has a well-defined boundary in most filters except FQ727N and F631N, where minimal gas opacity and reduced sensitivity to small haze particles means that the contrast is dominated by deeper cloud features. Scans were conducted across the GRS at the core central latitude and longitudes, averaged over ±0.2°. These are plotted in Figure 6 for each of the higher-contrast filters. Despite the varying

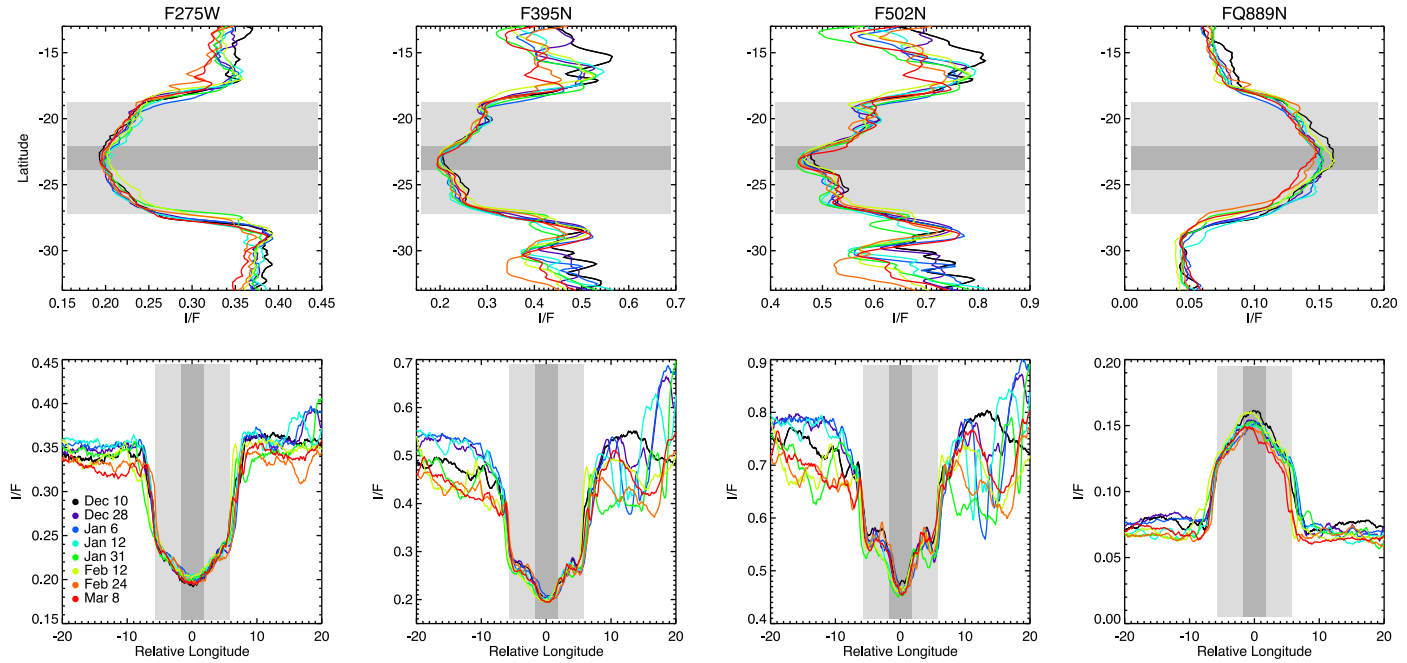

Figure 6. GRS brightness over time. Top: latitude scans, averaged over the central longitude, in the F275W, F395N, F502N, and FQ889N filters for each date. Bottom: longitude scans, averaged over the central latitude, in the same filters for each date. The gray shaded areas correspond to the average red ellipse and core sizes.

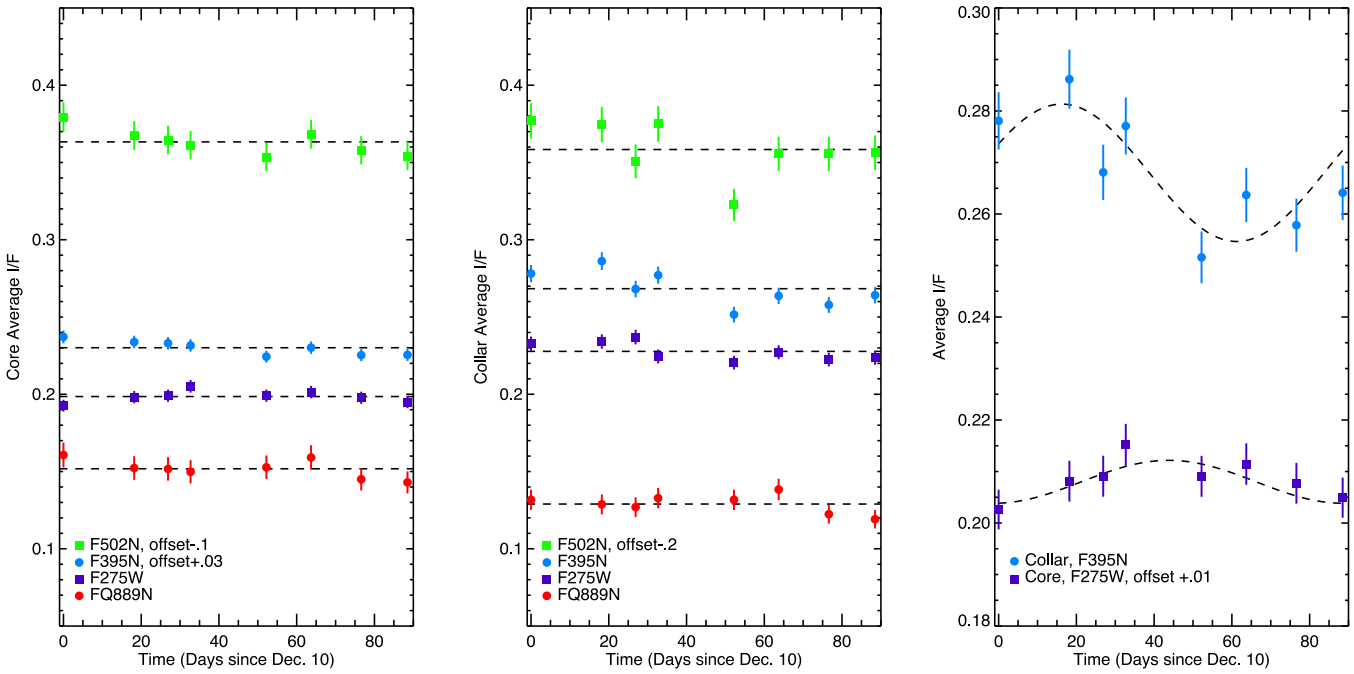

Figure 7. GRS brightness over time. Left: core brightness for each filter in Figure 6; the F395N and F631N filters were offset for clarity. Dashed lines indicate mean values. Middle: collar brightness for each filter in Figure 6; F631N was offset for clarity. Dashed lines indicate mean values. Right: F275W core brightness and F395N collar brightness showed the best correlations with a 90 days oscillation.

appearance in Figures 2 and 3, the interior of the GRS does not show large temporal variations in brightness or scan shape.

To further study variations, smaller area averages were performed for the core ($\pm 0.1^\circ$ in latitude and longitude); see Figure 7. Most of the variations are small, within the uncertainties of the I/F, particularly in the FQ889N filter. A similar comparison was made for a region in the collar west of the core, again averaged over $\pm 0.1^\circ$ in latitude and longitude (Figure 7, middle panel). This location was chosen because streams of material tend to enter on the south and east, so this area is more representative of the mixed collar material.

Despite the small variations, the brightness values were checked for correlation with a 90-day oscillation. The only plausible correlation of core brightness with a 90-day oscillation ($r > 0.7$) occurs for the core in F275W ($r = 0.82$), again nearly anticorrelated with the drift rate oscillation (phase lag of 165°; Figure 7, right panel). For the collar, the only brightness with a 90-day oscillation was in F395N ($r = 0.80$) with an 85° phase lag from the drift rate oscillation. The collar

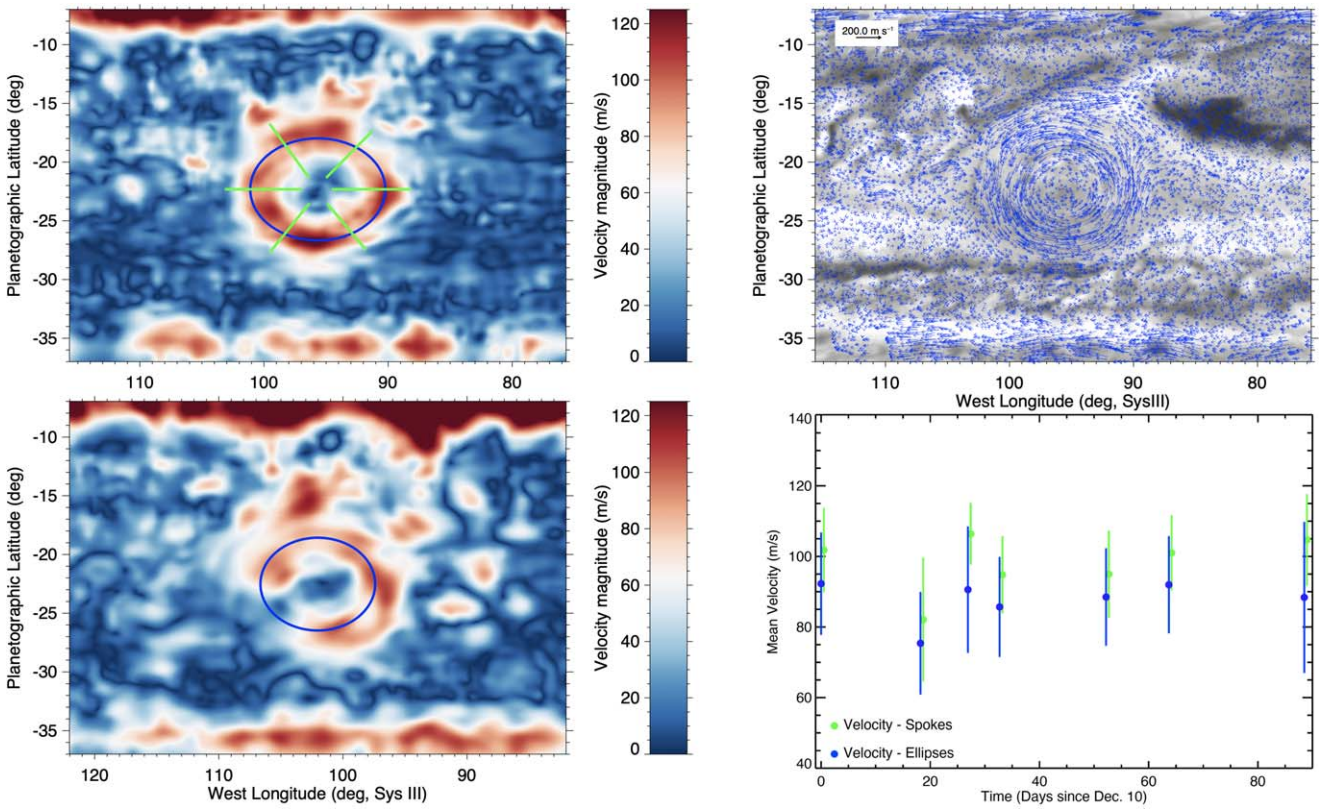

Figure 8. GRS velocity fields over time. Top left: the December 10 velocity magnitude diagram clearly shows the high-velocity collar; velocities can be averaged along a best-fit ellipse or radially on spokes following M. H. Wong et al. (2018). Top right: individual velocity vectors from December 10 plotted across the entire field show the center of the GRS has little motion. Bottom left: the December 28 velocity magnitude diagram shows that vectors could not be found in some regions of the high-velocity collar, resulting in a lower overall average velocity. Bottom right: some variability is evident, with minimum and maximum mean speeds differing by about 20 m s^{-1}, but the differences are only marginally significant (with a mean uncertainty on the speed at each epoch of about 13 m s^{-1}), and the pattern of variability did not follow a 90 days sinusoidal oscillation.

F275W and F502N brightness also showed moderate correlation ($r = 0.68$ and 0.69, respectively) to a 90-day oscillation (not plotted), with a similar phase lag of 90° and 60°, respectively.

6. GRS Mean Wind Speed and Relative Vorticity

As discussed above, the GRS high-speed collar velocity was measured along spokes and by averaging over the best-fit ellipse to the high-speed ring; see Figure 8. Velocities on some dates were poorly fit due to imaging geometries and time separations, resulting in larger uncertainties. The mean velocities are in agreement with prior studies (A. A. Simon et al. 2018; A. Sánchez-Lavega et al. 2021; M. H. Wong et al. 2021), though no obvious oscillation is seen in Figure 8. Full two-dimensional wind fields are available from the archive repository for each date that ACCIV successfully retrieved a velocity field (M. H. Wong 2021). Successful velocity fields were subjectively identified as those without excessive defects such as spurious velocity patterns (convergence/divergence) or "bald spot" patches lacking retrieved velocity vectors.

We calculated separate averages of the GRS relative vorticity over the dark central core (as defined photometrically), as well as the surrounding collar. The relative vorticity averages are reported in Table 4. Using the photometrically defined core, we did not find that the core was less anticyclonic (or even counterrotating cyclonically) compared to the collar, unlike previous observational results (e.g., D. Choi et al. 2007; S. Shetty et al. 2007; M. H. Wong et al. 2021; A. Zhang & P. S. Marcus 2024). The lack of core counterrotation using the photometric core boundary is likely due to differences in resolution. Although the output velocity fields are gridded at a resolution of 0.1° per map pixel, fluctuations in the velocity fields (Figure 8) suggest a much cruder effective resolution on the order of 2°, or ∼2500 km. This is comparable to the dimensions of the photometric core (Table 2), which itself is not a perfect ellipse (Figure A2). Thus, the average vorticity value in the core is highly sensitive to the relative placement of the core boundary and the fluctuations in the velocity field. Additionally, the mean vorticities may be affected by differences in the altitudes of relevant clouds and hazes. Cloud-tracked winds depend on opacity variation in red wavelengths, which can penetrate overlying hazes to detect variations in the ammonia cloud deck (and deeper). The dark core, on the other hand, is primarily detected due to spatial variation in blue absorption, most likely an effect of chromophore haze opacity (e.g., E. K. Dahl et al. 2021; A. Anguiano-Arteaga et al. 2023).

7. Relative Cloud Structure Variations

A recent study of color and cloud structure using WFC3 data from 2015 to 2021 found the GRS brightness showed significant short-term variation, with the overall trends previously noted from 2015 to 2018 reversing from 2018 to 2021 (A. Anguiano-Arteaga et al. 2023). These brightness variations were attributed to changes in the tropospheric and stratospheric hazes. A. Anguiano-Arteaga et al. (2023) also

Table 4
GRS Velocity Parameters

Date	Mean Velocity ($m\ s^{-1}$)		Vorticity ($10^{-5}\ s^{-1}$)		
	Ellipse	Spokes	Collar	Core	Background
2023 Dec 10	92.3 ± 14.5	101.8 ± 11.9	−4.0 ± 0.9	−5.1 ± 1.0	−1.5 ± 0.5
2023 Dec 28	75.4 ± 14.5	82.1 ± 17.5	−3.4 ± 1.0	−5.2 ± 0.8	−1.6 ± 0.5
2024 Jan 6	90.6 ± 17.9	106.4 ± 8.7	−5.2 ± 0.9	−5.2 ± 1.0	−1.4 ± 0.5
2024 Jan 12	85.7 ± 14.2	94.8 ± 10.9	−4.6 ± 0.7	−5.3 ± 1.1	−1.8 ± 0.5
2024 Jan 31	88.5 ± 13.8	95.0 ± 12.3	−4.3 ± 0.7	−5.3 ± 0.8	−1.4 ± 0.5
2024 Feb 12	92.0 ± 13.8	101.0 ± 10.7	−4.2 ± 0.8	−5.3 ± 1.0	−1.9 ± 0.5
2024 Mar 8	88.4 ± 21.4	104.7 ± 13.0	−5.0 ± 1.1	−4.4 ± 1.6	−1.8 ± 0.5

computed color (F395N/F631N, CI) and altitude/opacity (FQ889N/F275W, AOI) indices, finding a range for the GRS core of 0.19–0.3 and 0.78–1.07, respectively, from 2015 to 2021. For the collar the CI ranged from 0.25 to 0.37 and the AOI from 0.64 to 0.91 from 2015 to 2021. In our 90 days data set, the core F275W and FQ889N brightness in Figure 7 vary by ∼5% and 13%, respectively, over 90 days and are consistent with the I/F values observed in 2018. We find a CI = 0.26–0.28 and AOI of 0.73–0.83 for the core, and CI = 0.32–0.36 and AOI = 0.53–0.61 for the collar. While the color index is about the same as in the longer-term study, the AOI is lower for the core and more so for the collar, perhaps indicating haze opacity or altitude has changed since 2021.

Another indicator of cloud structure variation is the appearance of the interior dark lanes (or "large dark thin filaments" as described in A. Sanchez-Lavega et al. 2018) visible in Figure 2. The increased dark lane contrast since 2018 could indicate a clearing of upper tropospheric clouds, and this is supported by 5 μm data that indicate these lanes are bright in thermal emission (see Figure A3, and Figure 10 in M. H. Wong et al. 2020). Over the dates shown in Figure 2, the lanes are visible on almost every date and mark part of the GRS edge on January 31 through March 8, so they are not oscillation dependent. While the significance of more frequent dark lane appearance is as of yet unknown, their appearance on the GRS periphery indicate that the upper red clouds of the GRS are disconnected from the vortex below it, at least at that location.

UV images and false-color composites using the FQ889N and FQ727N filters were used to further highlight altitude variations across the GRS and its surroundings; see Figure 9. In a composite with FQ889N, FQ727N, and F631N in the RGB channels, higher clouds appear pink. First, the high material over the GRS is offset from the deeper vortex; December 10 and January 31 are very striking in their lack of high cloud in the northwest quadrant. Streamer material on January 31 also appears to be high altitude. Reversing the filter order brings out deep cloud structures indicative of the base of towering convective structures (A. R. Vasavada et al. 1998; P. J. Gierasch et al. 2000; M. H. Wong et al. 2023a), as seen in Figure 9 (right column) as reddish clouds. Deep convective activity in the GRS wake is also prominent on December 10 and January 31, and to a lesser extent on January 12 and February 12, but unfortunately we do not have the weaker methane band coverage on all dates to check for any correlations. The lack of deep structures visible inside the GRS in image composites including the continuum and weak methane band is due to the large haze opacity (M. H. Wong et al. 2023a) over the entire GRS, including the dark lanes as well as more cloudy regions.

Lastly, convective activity in the surrounding environment can result in GRS collar brightness variations; as the GRS drifts and its interactions with the surroundings change, more fresh cloud can be drawn into the GRS flow field to change the collar color (P. V. Sada et al. 1996). The collar brightness shows a phase lag of 90° (22.5 days) from the drift oscillation, suggesting the dynamical timescale for external material to become entrained into the GRS flow plus the several day rotation period of the interior of the spot to mix the cloud into the collar (A. A. Simon et al. 2018; M. H. Wong et al. 2021). Unfortunately, the limited data do not allow us to draw a definitive connection between convective features, the offset high-altitude clouds, and the oscillation.

8. Discussion

The cause of the GRS's 90-day oscillation is still unknown, even though such oscillations are common to other vortices on Jupiter and Neptune. It has been suggested in the past that the GRS's placement in the wind shear (latitude) varies, contributing to the drift rate in an oscillatory manner (P. Marcus 1993; J. M. Trigo-Rodriguez et al. 2000; T. Asada & I. Miyazaki 2006). First, the longitudinal drift of the GRS is partially driven by the ambient flow (P. Marcus 1993). The zonal flow, V_x, surrounding the GRS has a nearly constant shear, σ:

$$\sigma \equiv dV_x/dy,$$

where y is the local north–south coordinate. The drift rate, $V_{\rm drift}(y)$, would be a combination of the background shear and the zonal velocity at the core latitude; for example, at −23°,

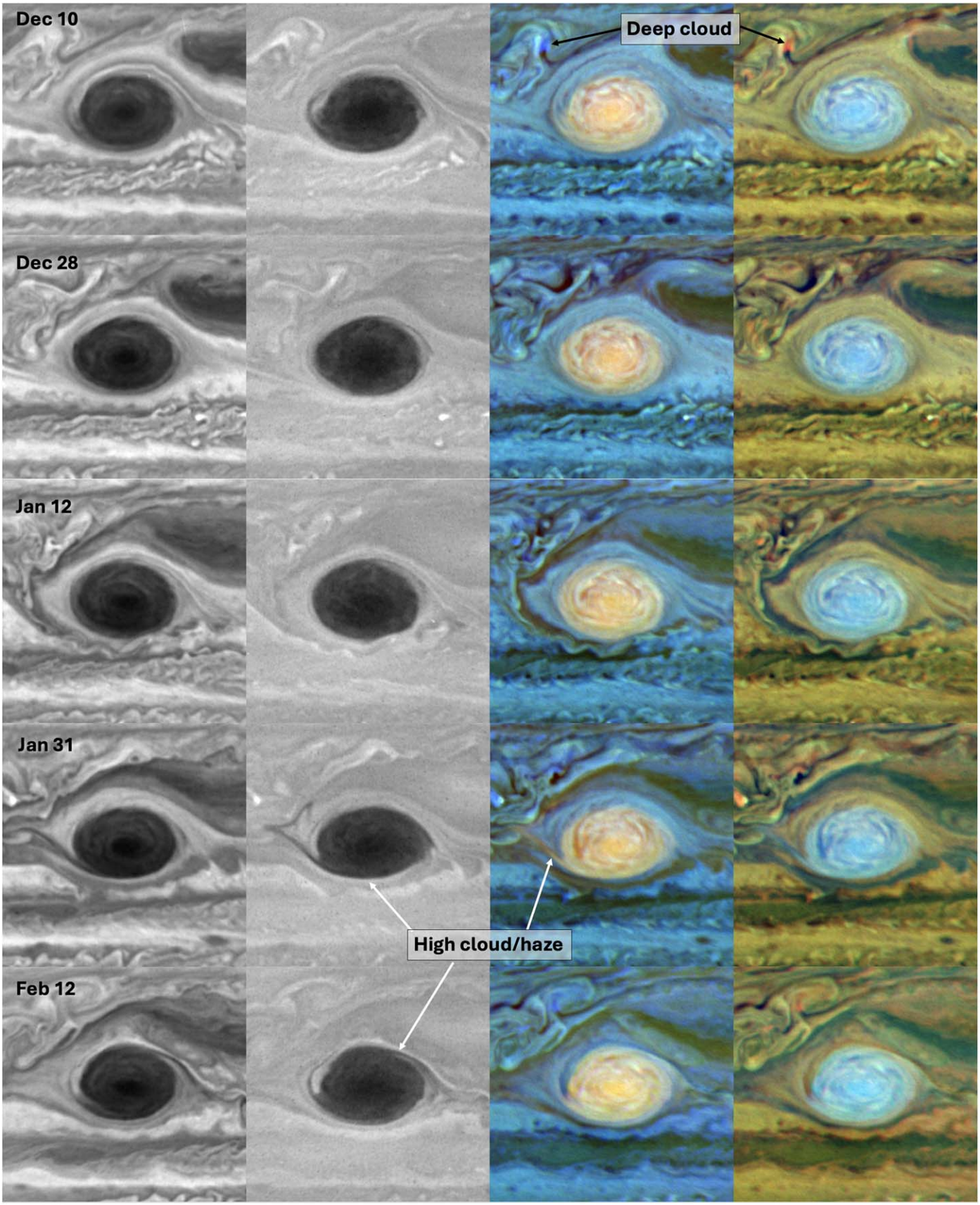

Figure 9. GRS altitude and false-color composite maps. Left column: GRS in F395N shows the extent of redder material (blue absorption). Second column: F275W highlights the highest-altitude material. Third column: false-color composite of the FQ889N (R), FQ727N (G), and F631N (B) filters further highlights the GRS as high (pink shades), with entering high-altitude streamer material. Right column: reversed false-color composite with the F631N (R), FQ727N (G), and FQ889N (B) filters highlights the deep convective storms in the wake in red, with streamers visible in pale blue.

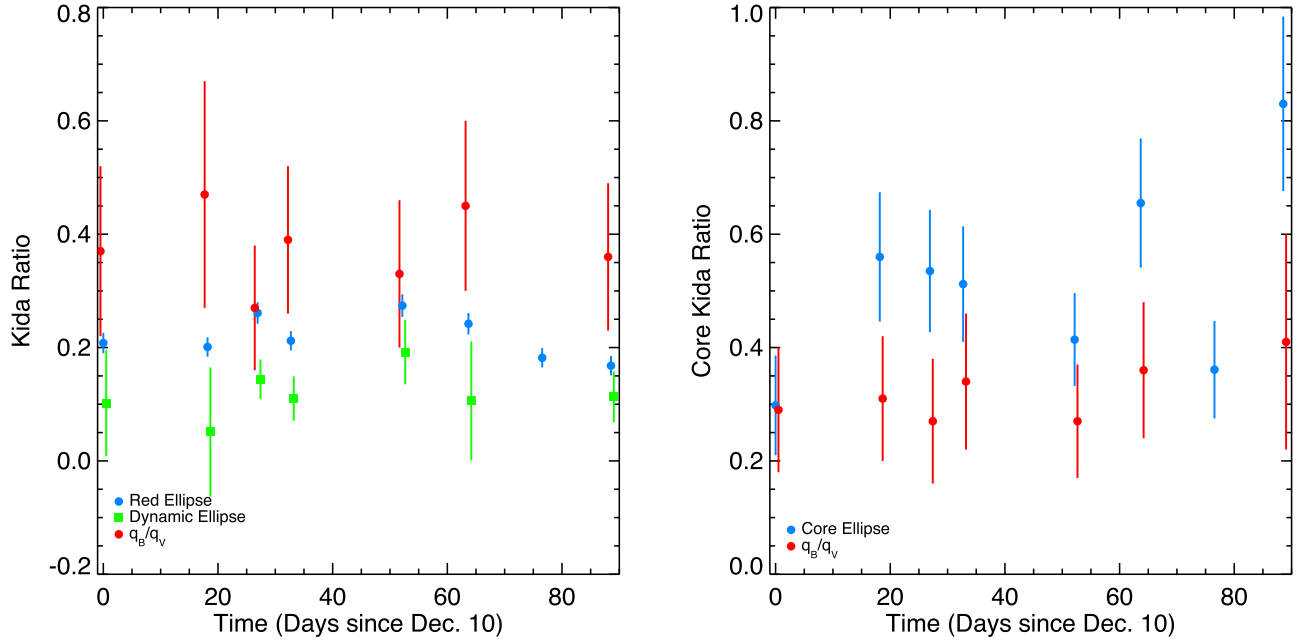

Figure 10. Comparison of vorticity ratios to aspect ratio using the Kida relation. Left: the GRS red ellipse (blue points) or dynamical size (green points) only overlap with the vorticity ratio (red points) on the January dates, even with the large error bars; data were offset by 0.5 days for clarity. Right: the same comparison for the core ellipse and vorticity ratio shows they also disagree.

$V_{\rm drift} \approx V_{\rm x}(-23°) + \sigma y + C$, where C is a contribution from any other source, of either sign, such as a standing wave. The zonal velocity at $-23°$ is constant and near zero, but the shear has likely increased slightly as the GRS has shrunk, in agreement with an overall faster drift rate over time (A. A. Simon et al. 2018). Ignoring the zonal wind deflection around the GRS, the core and red ellipse north edge latitudes found in Table 2 give a background zonal wind shear of -6.3 to $-9.7 \times 10^{-6}\,{\rm s}^{-1}$ over these dates. The average GRS drift rate is around 4–5 m s^{-1}, much slower than the shear values alone would imply ($\sim$40 m s^{-1}), indicating other factors also play a role in the GRS's total drift rate.

J. M. Trigo-Rodriguez et al. (2000) predicted a latitude oscillation of $\sim$0.16°, using their measured longitude oscillation amplitude (1.2°) and zonal wind velocities. However, their latitude measurements largely gave null results. A follow-up study by T. Asada & I. Miyazaki (2006) used 10 months of ground-based telescopic data to fit longitudinal oscillations (0.5°–0.6° amplitude) with different periods. They found a possible latitudinal oscillation (0.3° amplitude), though it was at the limit of their spatial resolution, and correlation coefficients were low. In these new Hubble data, the longitude oscillation has an amplitude of about 0.9°, and there is no definitive oscillation in latitude. However, the GRS latitude does change by at least a few tenths of a degree (Figure 3), in agreement with T. Asada & I. Miyazaki (2006). The red ellipse semiminor axis size also shows no obvious oscillation, nor correlation with latitude that might indicate that the oscillation is driven by changes in background shear.

This study is the first to note an oscillation of the semimajor axis, the core size, and the near-UV F275W core brightness, all anticorrelated with drift rate. The GRS and its core are largest and brightest when it is drifting the slowest. The GRS may interact with the surrounding flow more when accelerating and then relax toward equilibrium in between. The radiative time constant on Jupiter is long (on the order of years), but the dynamical timescale for convective overturning can be quite short, on the order of a few days (e.g., F. M. Flasar 1989). The core F275W brightness increases as the spot and core expand, indicating a decrease in haze, due to either optical depth or particle size, on those dates. This is in line with prior observations that suggested vortex stretching when compressed, but a single oscillation cycle is insufficient to definitively attribute this change to any specific forcing process.

In the past, it was suggested that the GRS followed the Kida relation, as in the Voyager epoch its aspect ratio roughly matched that expected from the ratio of background and vortex vorticity (L. M. Polvani et al. 1990):

$$\frac{q_{\rm B}}{q_{\rm V}} = \frac{1-\lambda}{\lambda(1+\lambda)},$$

where $q_{\rm B}$ is the background vorticity, $q_{\rm V}$ is the vortex vorticity, and λ is the inverse of the aspect ratio. The calculated GRS vorticities are listed in Table 4, and the background vorticity was chosen based on the northern edge of the red ellipse in Table 1 rather than a constant value, though it makes little difference. We assumed an uncertainty on the background vorticity of $5 \times 10^{-6}\,{\rm s}^{-1}$, as it can vary over time (A. A. Simon et al. 2018). As shown in Figure 10 (left panel), this relation does not hold for the dynamical or red ellipses, other than perhaps when the GRS is at its largest extent (the middle of the oscillation). The core aspect ratio also fails to match the vorticity ratio (Figure 10, right panel).

The Kida relation also predicts an axial tilt variation that correlates with aspect ratio, and Neptune's GDS was shown to oscillate in shape/axis in Voyager data according to this relation (B. A. Smith et al. 1989; L. M. Polvani et al. 1990). Similar GRS movies from Voyager did not show an obvious axial motion. In these Hubble data, the red cloud ellipse fits are not useful for defining tilts given the uncertainty in shape due

to the streamers of material; it is also possible that the full GRS vortex cannot oscillate as much as the GDS, as it is more confined by more tightly spaced zonal jets. However, it should be noted that the core shape does show a varying tilt, as seen in Figure A2. The tilt appears to be somewhat random, however: No oscillation can be discerned on the data sets with 10 hr separations, while other small spots south of GRS do tilt over 10 hr.

The Kida equations assume a simple quasi-geostrophic, or two-layer, structure that may not apply to the GRS. The GRS has a height of ∼150–500 km (D. Lemasquerier et al. 2020; M. Parisi et al. 2021), so it is likely that we are observing winds above the vortex midplane where the relationships would apply (M. H. Wong et al. 2023b). Beside the question of how deep the midplane lies, we also do not know the speed of GRS winds nor the background shear at the midplane depth. Lastly, the overall GRS dynamics may be more complicated, so that a two-dimensional picture at the midplane is also not sufficient to describe the system (A. Zhang & P. S. Marcus 2024). Smaller Jovian spots and the Neptune dark spots may be thinner, such that the Kida equations are more easily applied.

9. Conclusions

Using Hubble data spanning 88.5 days, we completed a detailed study of the GRS size, shape, brightness, color, and vorticity over a full oscillation cycle. We find that the GRS's width, aspect ratio, and core UV brightness all oscillate on the same 90-day timescale (the online version of Figure A5 provides a visual animation of these simultaneous oscillations):

1. The GRS width and core size are anticorrelated with drift rate, with the largest sizes occurring when it is drifting the slowest.
2. The core UV brightness is also highest when the spot is largest, indicating less haze absorption.
3. Despite the observed oscillations, the GRS does not obey the Kida relation.

Future studies would benefit from longer and more frequent time coverage of the GRS, particularly as it continues to decrease in size. In principle, the vast database of amateur observations and GRS measurements could be mined to uncover more oscillations in size and shape.[5] However, the width variation found here is ∼0.3° of longitude over ∼2 weeks, while the scatter in the amateur data approaches 1°, which is insufficient to discern this oscillation. Now that the size oscillation is known, it is possible that future analyses might be able to draw out this cycle from the high-cadence amateur data. Other high-resolution data sets might also identify other Jovian parameters that indicate the underlying cause of the oscillation. The results of future high-cadence observations could be particularly informative during times when the 90-day oscillation is perturbed (A. Sánchez-Lavega et al. 2021).

Extending the imaging wavelength coverage, particularly into long wavelengths, would also be useful. Using wavelengths that can sense deeper levels would also be valuable for determining if wind velocities are changing below the GRS's cloud tops. Wind shear at altitudes above the HST cloud tracers can now be probed with JWST (R. Hueso et al. 2023; M. H. Wong et al. 2023b). High-spatial-resolution data at 5 μm and at radio wavelengths could be especially insightful as probes of deeper levels. Lastly, detailed circulation modeling of the GRS oscillatory behavior with these new characteristics may provide further insight on the deeper dynamics.

Acknowledgments

This article includes observations made with the NASA/ESA Hubble Space Telescope obtained from the Space Telescope Science Institute, which is operated by the Association of Universities for Research in Astronomy, Inc. (AURA), under NASA contract NAS 5–26555. These observations are associated with program(s) GO16995, GO17275, and GO17294. The authors were supported by a grant associated with program GO17294. We gratefully acknowledge the Hubble schedulers and our program coordinators for enabling the high-cadence data set that made this study possible. The Hubble data used in these analyses can be retrieved from the MAST archive at doi:10.17909/e04n-w807.

Appendix
Supporting Material

The supporting material includes Figures A1, A2, and A3, and the online animated Figures A4 and A5. Figures A1 and A2 display the best-fit ellipses used in the analyses throughout the paper. Figure A3 shows examples from 2018 of the dark lane features discussed in the paper, and how they tie to thermal IR emission. Animated Figures A4 and A5 are provided to help visual interpretation of the changes over the 90-day cycle. Figure A4 is an animated version of the images shown in Figure 2, while Figure A5 is a cartoon animation depicting all of the simultaneous GRS changes within an oscillation cycle.

[5] For example, http://jupos.hier-im-netz.de/.

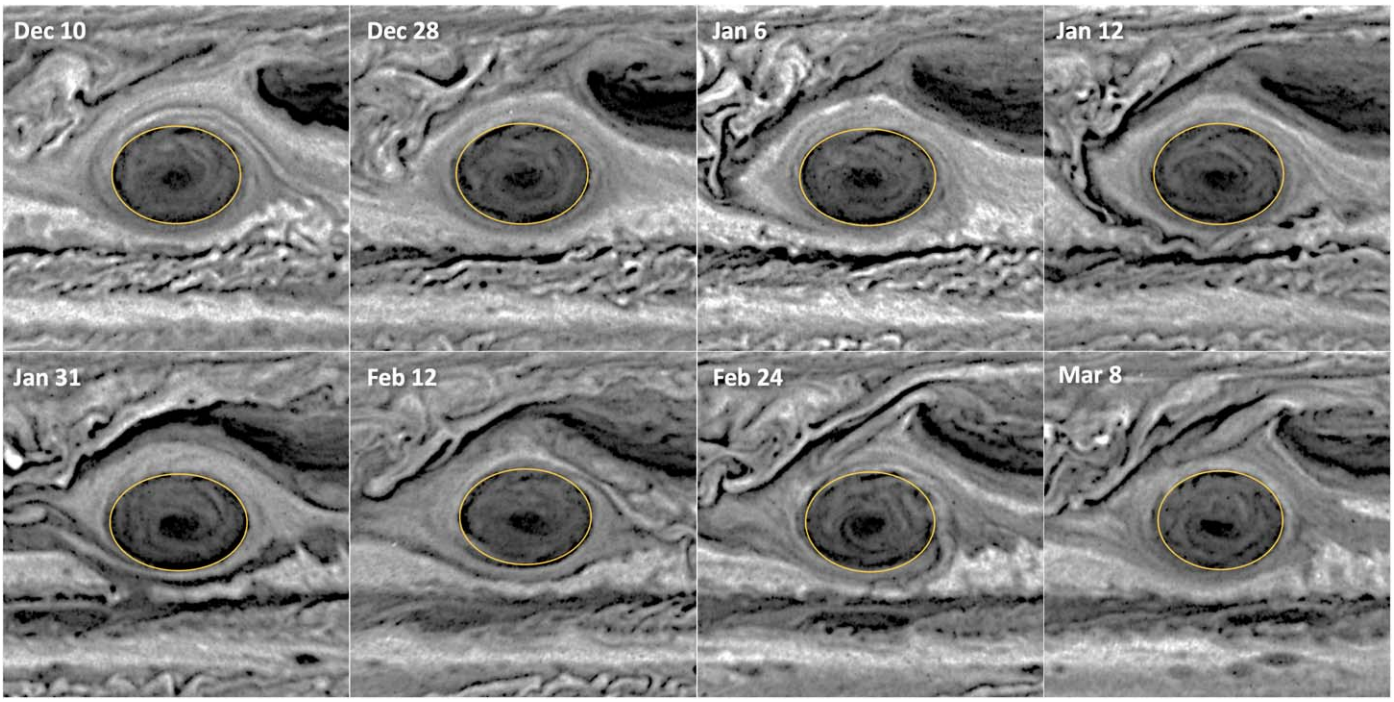

Figure A1. GRS cloud edge elliptical sizes on enhanced F502N image maps. For each date, the F502N GRS map was first lightly contrast enhanced and sharpened with an unsharp mask. The ellipse that best contained the red (dark) cloud area was visually identified. This was compared with the same images after further contrast enhancement and sharpening, as well as against brightness contours, to ensure a good match to the vortex edges.

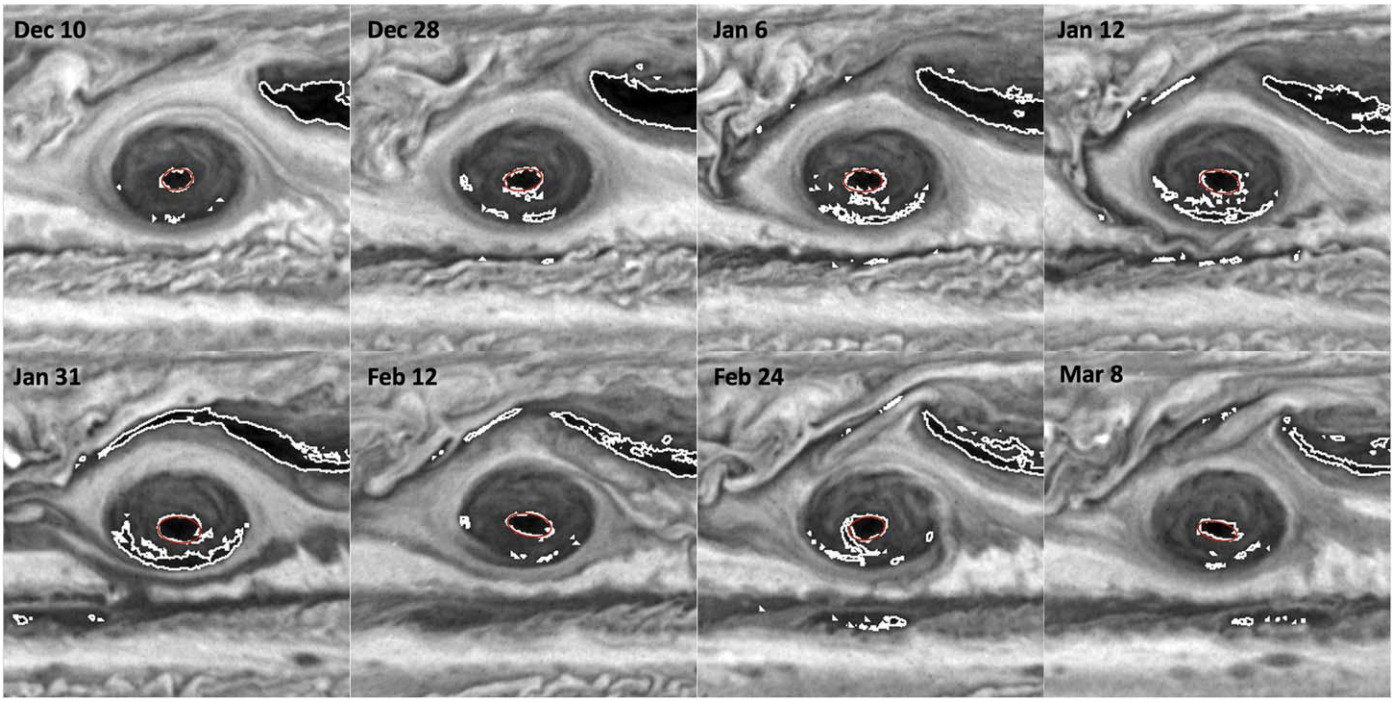

Figure A2. GRS core ellipse fitting on unsharp masked F502N images. For each date, images were scaled to the same contrast, and contours of $I/F = 0.5$ were identified (white lines). The ellipse (red) that best overlaid the contours was then used to determine size and orientation.

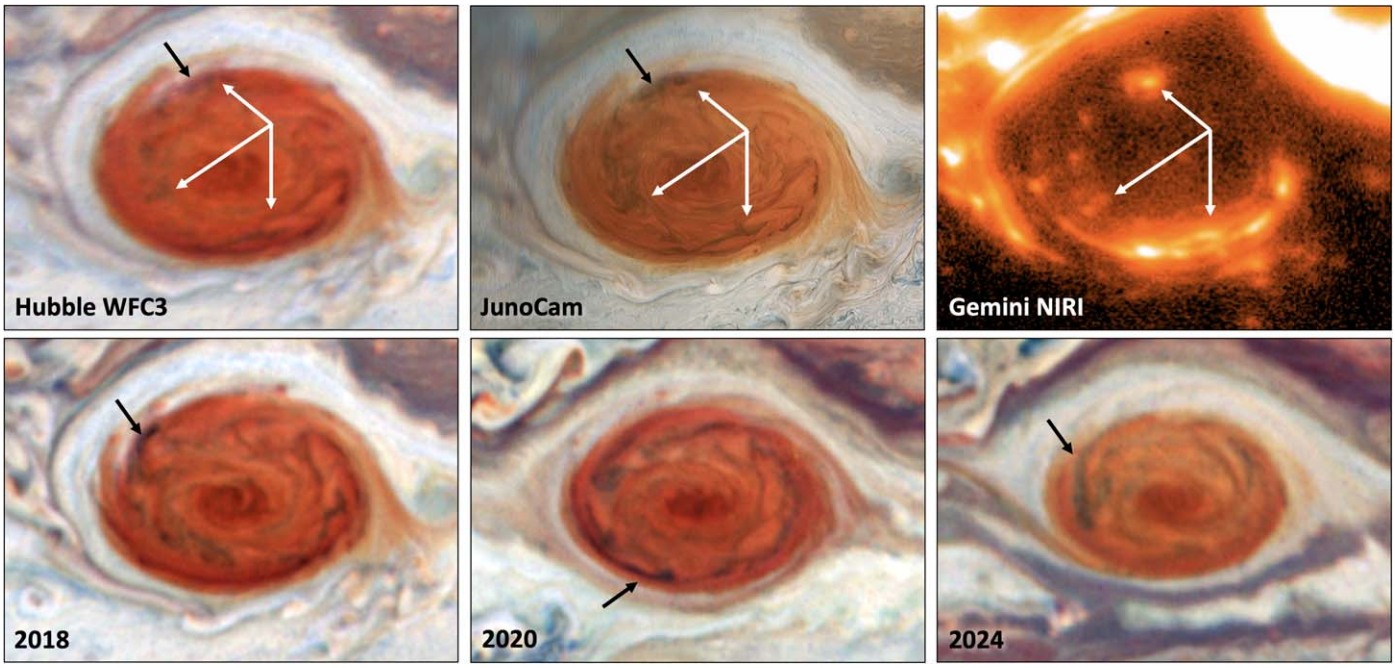

Figure A3. GRS dark lanes and corresponding IR hot spots. Top: near-simultaneous Hubble, Juno, and Gemini images from 2018 April 1. Left: Hubble data at ∼09:00 UT, with arrows marking dark lanes. Middle: JunoCam image (from NASA PIA21985) taken at ∼10:00 UT and the same features noted. Right: Gemini NIRI data taken at ∼10:50 UT, showing 5 μm IR hot spots at the same locations as the interior dark features (from M. H. Wong et al. 2020). Bottom: Hubble WFC3 images showing examples of the more frequent high-contrast dark lanes seen since 2018.

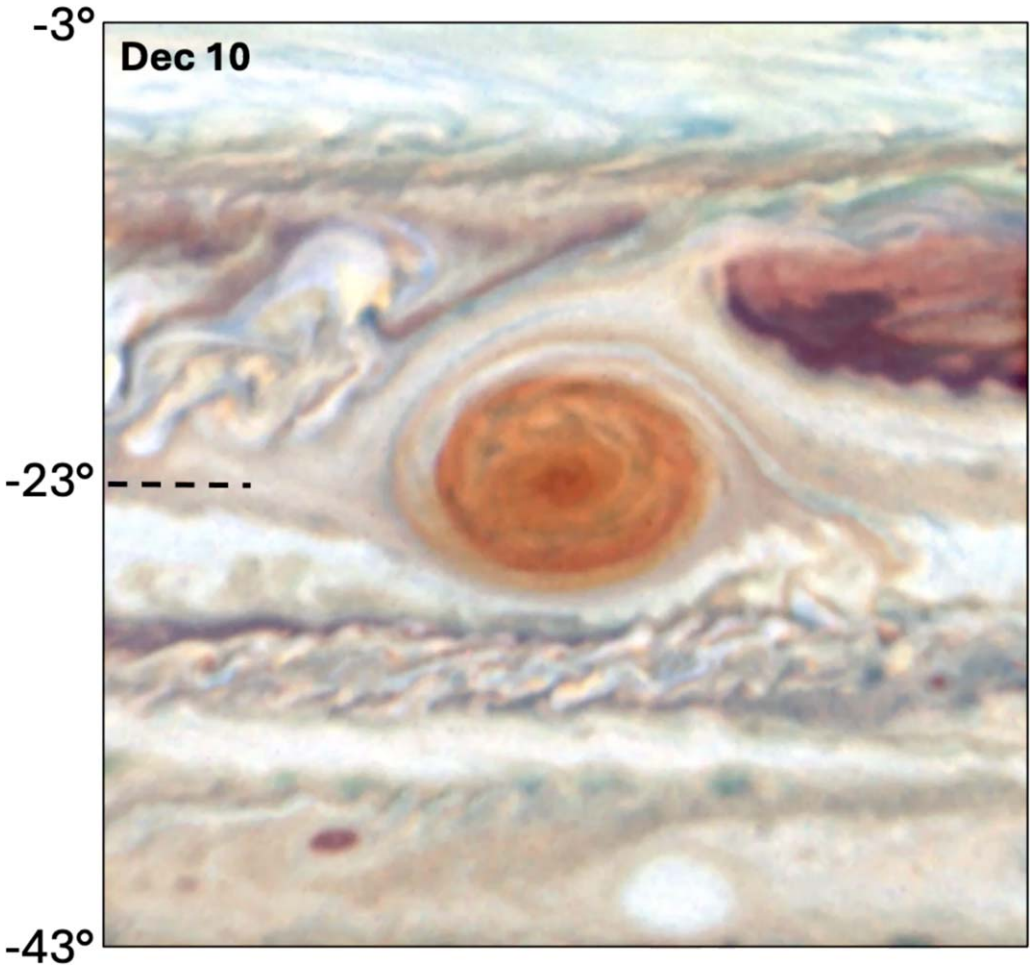

Figure A4. An animation of the GRS evolution over a 90 days cycle. For each date, the GRS was mapped at −23° latitude and the GRS longitude and mapped over ±20° in both dimensions in the F631N, F502N, and F395N filters. These are assembled into color images with one time step per date. The internal features, size, and shape are observed to change from date to date.

(An animation of this figure is available in the online article.)

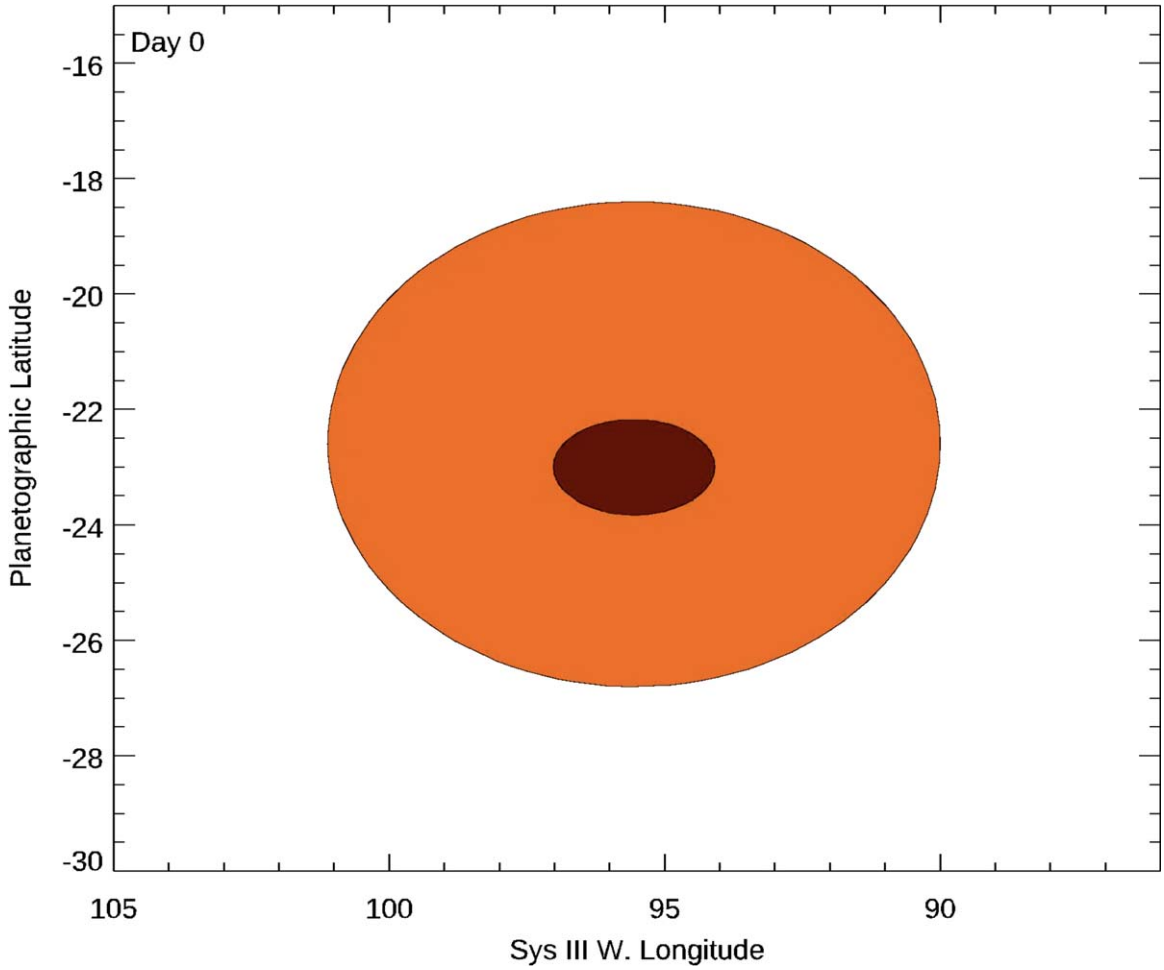

Figure A5. Simultaneous oscillations within the GRS. This movie animates the sinusoidal oscillation in drift rate (Figure 4), red ellipse semimajor axis size (Figure 5), and core semimajor and semiminor axes (Figure 5) over the 90-day cycle. The color of the ellipse and core also vary sinusoidally over the cycle (Figure 7), though the color is exaggerated here.

(An animation of this figure is available in the online article.)

ORCID iDs

Amy A. Simon https://orcid.org/0000-0003-4641-6186
Michael H. Wong https://orcid.org/0000-0003-2804-5086
Patrick G. J. Irwin https://orcid.org/0000-0002-6772-384X

References

Anguiano-Arteaga, A., Pérez-Hoyos, S., Sanchez-Lávega, A., et al. 2023, JGRE, 128, e2022JE007427
Asada, T., & Miyazaki, I. 2006, EP&S, 58, 905
Asay-Davis, X. S., Marcus, P., Wong, M. H., & de Pater, I. 2009, Icar, 203, 164
Asay-Davis, X. S. 2015, GitHub Repository, https://github.com/xylar/acciv
Choi, D., Banfield, D., Gierasch, P., & Showman, A. 2007, Icar, 188, 35
Dahl, E. K., Chanover, N. J., Orton, G. S., et al. 2021, PSJ, 2, 16
Dowling, T. E. 1995, AnRFM, 27, 293
Flasar, F. M. 1989, Temporal Behavior of Jupiter's Meteorology in Time Variable Phenomena in the Jovian System, NASA Special Publication Series NASA-SP-494, NASA/Goddard Space Flight Center, 324
Gierasch, P. J., Conrath, B. J., & Magalhaes, J. A. 1986, Icar, 67, 456
Gierasch, P. J., Ingersoll, A. P., Banfield, D., et al. 2000, Natur, 402, 628
Hammel, H. B., Lockwood, G. W., Mills, J. R., & Barnet, C. D. 1995, Sci, 268, 1740
Holton, J. 1992, An Introduction to Dynamic Meteorology (3rd ed.; Cambridge, MA: Academic Press)
Hsu, A., Wong, M. H., & Simon, A. A. 2019, AJ, 157, 152
Ingersoll, A., Dowling, T. E., Gierasch, P. J., et al. 2004, Jupiter: The Planet Satellites and Magnetosphere (Cambridge: Cambridge Univ. Press)
Hueso, R., Sánchez-Lavega, A., Fouchet, T., et al. 2023, NatAs, 7, 1454
Kida, S. 1981, JPSJ, 50, 3517
Lebeau, R., & Dowling, T. E. 1998, Icar, 132, 239
Lemasquerier, D., Facchini, G., Favier, B., & Le Bars, M. 2020, NatPh, 16, 695
Li, L., Ingersoll, A. P., Vasavada, A. R., et al. 2006, JGRE, 111, E04004
Marcus, P. 1993, ARA&A, 31, 523
Mitchell, J. L., Beebe, R. F., Ingersoll, A. P., & Garneau, G. W. 1981, JGR, 86, 8751
Morales-Juberias, R., Simon, A. A., & Cosentino, R. G. 2022, Icar, 372, 114732
Parisi, M., Kaspi, Y., Galanti, E., et al. 2021, Sci, 374, 964
Peek, B. M. 1958, The Planet Jupiter (London: Faber and Faber)
Polvani, L. M., Wisdom, J., DeJong, E., & Ingersoll, A. P. 1990, Sci, 249, 1393
Read, P., Gierasch, P. J., Conrath, B. J., et al. 2006a, QJRMS, 132, 1577
Rogers, J. H. 1995, The Giant Planet Jupiter (Cambridge: Cambridge Univ. Press)
Sanchez-Lavega, A., Hueso, R., Eichstadt, G., et al. 2018, AJ, 156, 162
Sánchez-Lavega, A., Anguiano-Arteaga, A., Inurrigarro, P., et al. 2021, JGRE, 126, e2020JE006686
Sánchez-Lavega, A., García-Melendo, E., Legarreta, J., et al. 2024, GeoRL, 51, e2024GL108993
Sada, P. V., Beebe, R. F., & Conrath, B. J. 1996, Icar, 119, 311
Schultz Tokos, K., & Rossby, T. 1991, JPO, 21, 879
Shetty, S., Asay-Davis, X. S., & Marcus, P. S. 2007, JAtS, 64, 4432
Shetty, S., & Marcus, P. S. 2010, Icar, 210, 182
Simon-Miller, A. A., Gierasch, P. J., Beebe, R. F., et al. 2002, Icar, 158, 249
Simon, A. A., Tabataba-Vakili, F., Cosentino, R., et al. 2018, AJ, 155, 151
Simon, A. A., Wong, M. H., & Orton, G. S. 2015, ApJ, 812, 55
Smith, B. A., Soderblom, L. A., Banfield, D., et al. 1989, Sci, 246, 1422
Solberg, H. G. 1969, P&SS, 17, 1573
Sromovsky, L. A., Fry, P. M., & Baines, K. H. 2002, Icar, 156, 16
Sutyrin, G. G. 2020, OcMod, 156, 101711

Trigo-Rodriguez, J. M., Sanchez-Lavega, A., Gomez, J. M., et al. 2000, P&SS, 48, 331
Vasavada, A. R., Ingersoll, A. P., Banfield, D., et al. 1998, Icar, 135, 265
Wong, M. H. 2011, in Proc. 2010 STScI Calibration Workshop (Baltimore, MD: STScI), https://www.stsci.edu/files/live/sites/www/files/home/events/event-assets/2010/_documents/2010-hst-calibration-workshop-booklet.pdf
Wong, M. H. 2021, Jupiter Great Red Spot Velocity Fields from HST/WFC3, MAST, doi:10.17909/t9-jfs3-p240
Wong, M. H., Bjoraker, G. L., Goullaud, C., et al. 2023a, RemS, 15, 702
Wong, M. H., Hueso, R., de Pater, I., et al. 2023b, AGUFM, P32B–08
Zhang, A., & Marcus, P. S. 2024, JFM, 984, A61
Wong, M. H., Marcus, P. S., Simon, A. A., et al. 2021, GeoRL, 48, e2021GL093982
Wong, M. H., Simon, A. A., Tollefson, J. W., et al. 2020, ApJS, 247, 58
Wong, M. H., Sromovsky, L. A., Fry, P. M., et al. 2022, Icar, 387, 115123
Wong, M. H., Tollefson, J., & Hsu, A. I. 2018, AJ, 155, 117